Science results from sixteen years of MRO SHARAD operations

Nathaniel E. Putzig [a,*], Roberto Seu [b], Gareth A. Morgan [c], Isaac B. Smith [c,d], Bruce A. Campbell [e], Matthew R. Perry [a], Marco Mastrogiuseppe [b], the MRO SHARAD team

[a] Planetary Science Institute, 405 Urban Street, Suite 300, Lakewood, CO 80228, USA
[b] Sapienza Università di Roma, Dipartimento di Ingegneria dell'Informazione, Elettronica e Telecomunicazioni, Via Eudossiana, 18, 00184, Roma, Italy
[c] Planetary Science Institute, 1700 E. Fort Lowell Road, Suite 106, Tucson, AZ 85719, USA
[d] York University, Lassonde School of Engineering, 4700 Keele St, Toronto, ON M3J 1P3, Canada
[e] Smithsonian Institution Center for Earth and Planetary Studies, MRC 315, PO Box 37012, Washington, DC 20013-7012, USA

ARTICLE INFO

ABSTRACT

In operation for >16 years to date, the Mars Reconnaissance Orbiter (MRO) Shallow Radar (SHARAD) sounder has acquired data at its nominal 300–450 m along-track and 3-km cross-track resolution covering >55% of the Martian surface, with nearly 100% overlap in coverage at that scale in the polar regions and in a number of smaller mid-latitude areas. While SHARAD data have opened a new window into understanding the interior structures and properties of Martian ices, volcanics, and sedimentary deposits up to a few kilometers in depth, they have also led to new revelations about the deeper interior and the behavior of the planet's ionosphere. Here we summarize the data collected by SHARAD over this time period, the methods used in the analysis of that data, and the resulting scientific findings. The polar data are especially rich, revealing complex structures that comprise up to several dozen reflecting interfaces that extend to depths of 3 km, which inform the evolution of Martian climate in the late Amazonian period. SHARAD observations of mid-latitude lobate debris aprons and other glacier-like landforms detect strong basal reflections and low dielectric loss, confirming that they are ice-rich debris-covered glaciers. In other mid-latitude terrains, SHARAD data demonstrate the presence of wide-spread ground ices, likely at lower concentrations. SHARAD signals also probe non-icy materials, mapping out stacked lava flows, probing low-density materials thought to be ash-fall deposits, and occasionally penetrating sedimentary deposits, all of which reveal the structures and interior properties diagnostic of emplacement processes. SHARAD signals are impacted by their passage through the Martian ionosphere, revealing variations in time and space of the total electron content linked with the remanent magnetic field. Advanced techniques developed over the course of the mission, which include subband and super-resolution processing, coherent and incoherent summing, and three-dimensional (3D) radar imaging, are enabling new discoveries and extending the utility of the data. For 3D imaging, a cross-track spacing at the nominal 3-km resolution is more than sufficient to achieve good results, but finer spacing of 0.5 km or less significantly improves the spatially interpolated radar images. Recent electromagnetic modeling and a flight test show that SHARAD's signal-to-noise ratio can be greatly improved with a large (~120°) roll of the spacecraft to reduce interference with the spacecraft body. Both MRO and SHARAD are in remarkably fine working order, and the teams look forward to many more years in which to pursue improvements in coverage density, temporal variability in the ionosphere, and data quality that promise exciting new discoveries at Mars.

1. Introduction

The Mars Reconnaissance Orbiter (MRO) mission began its primary science phase in October 2006. Over the ensuing 16 years of operations, the Shallow Radar (SHARAD) sounder has acquired data along 32,800 discrete orbit segments ("observations") that cover 55% of the planet's surface at a 3-km cross-track resolution (Fig. 1), with substantial overlap in coverage, especially in the polar regions. As a sounding radar, SHARAD's primary objective is to map dielectric interfaces to several hundred meters depth in the Martian subsurface and to interpret these

results in terms of the occurrence and distribution of rock, sediments, regolith, water, and ice (Seu et al., 2004). The SHARAD signal is also affected by its passage through the Martian ionosphere and thereby provides valuable information about its properties, such as the total electron content (TEC) and its variability in space and time (Campbell et al., 2011, 2014). In addition, the returned signals from the surface can be used to assess the surface roughness on the scale of SHARAD's wavelength (15 m) and the material properties within the uppermost ~5 m of the subsurface (Campbell et al., 2013). SHARAD provides complementary data to that obtained by MARSIS, the Mars Advanced Radar for Subsurface and Ionosphere Sounding onboard Mars Express, which operates in the 1–5 MHz range and thus has deeper penetration with an order of magnitude coarser vertical resolution (Picardi et al., 2004).

Due to practical limitations on returned data volume, SHARAD is operated in a targeted mode, wherein team members request acquisition of data along ground-track segments, most often delineated by fixed target boxes of varying sizes over specific areas of scientific interest. Early in the mission, a number of campaigns were carried out over regions and locations of the highest interest (e.g., both polar regions and mid-latitude volcanics and buried ices) as a means to ensure a rapid build-up of coverage over these areas. The team has also carried out targeting efforts for past, present, and proposed spacecraft landing sites. In this paper, we summarize the rich science return from the first 16 years of the mission, which has revealed the surface and subsurface properties of icy materials, volcanics, and sediments across Mars and contributes to a better understanding of the Martian ionosphere.

2. SHARAD observations and methods

Thorough descriptions of SHARAD's design and intended operations prior to the commencement of mission operations are given by Seu et al. (2004, 2007b). Here, we summarize the observations and methods to provide background sufficient for understanding the results obtained.

2.1. SHARAD observations

As the MRO spacecraft passes over a given targeted area along a segment of its orbit, SHARAD emits a series of electromagnetic signals and records the returned energy, using its 10-m dipole antenna for both transmitting and receiving. The data recorded on each such orbit segment constitutes a single observation, and thus the observations are of varying lengths that depend on target sizes and objectives. The transmitted radar signals are *chirps*, meaning that they are swept across a range of frequencies for a short period of time—in particular, SHARAD signals are downswept from 25 MHz to 15 MHz over 85 μs with a pulse repetition frequency (PRF) of 700.28 Hz. The 10 MHz bandwidth yields a *nominal* 15 m resolution (wavelength) in the range direction, which is the vertical direction for a nadir-sounding radar such as SHARAD. The SHARAD signals are subject to geometric spreading such that upon reaching the surface from MRO's orbit at ~300-km altitude, the Fresnel zone of the signal extends over a ~ 3 km circular area, establishing the *nominal* lateral resolution (Seu et al., 2007b). Upon encountering an interface with an abrupt change in dielectric properties—such as the Martian surface—a portion of SHARAD's signal energy is reflected and another portion is transmitted, with the speed of the transmitted radar signal and its wavelength altered by a factor of the square root of the
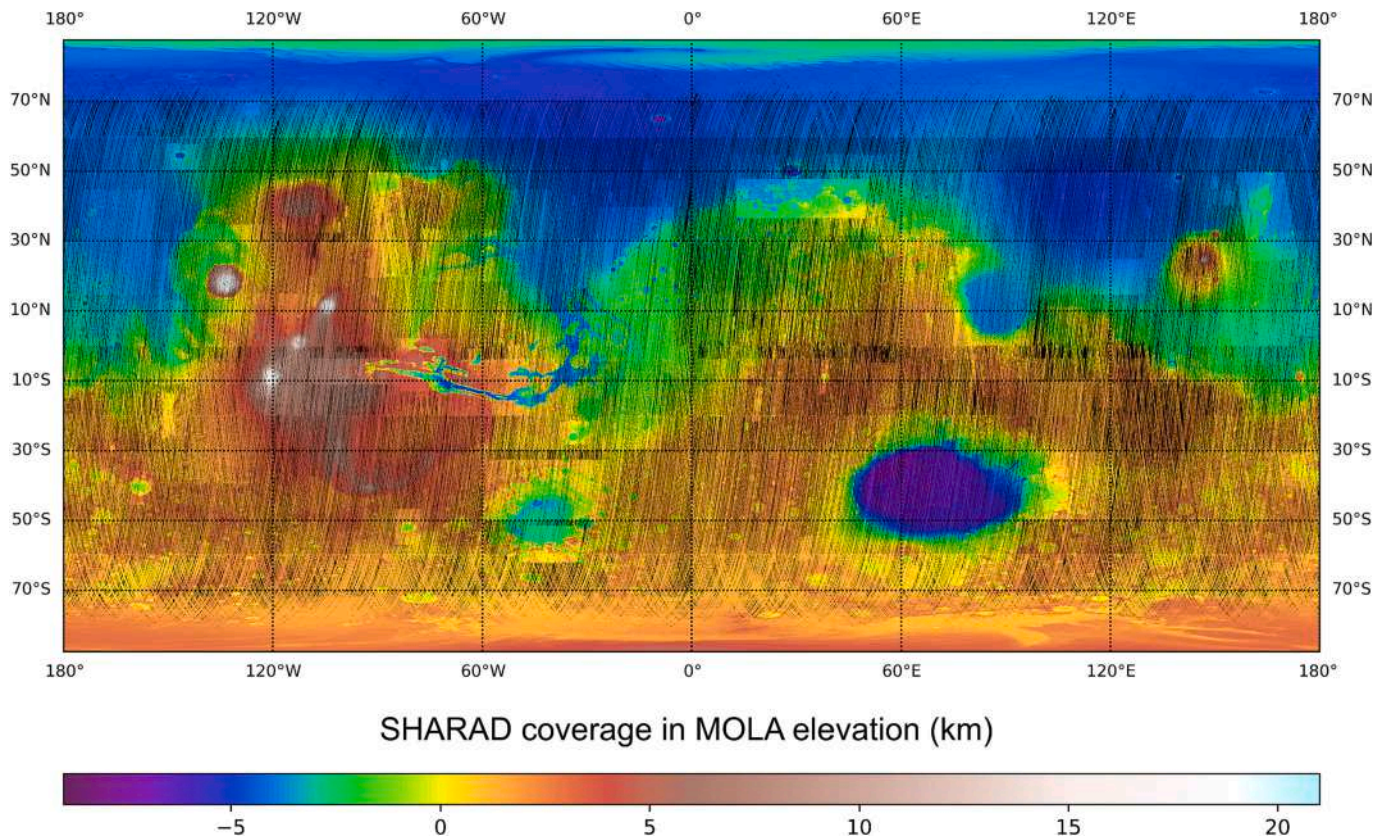

Fig. 1. SHARAD coverage, shown in MOLA colorized elevation (black areas have no coverage). Globally, coverage is 55% at 3 km per pixel from 32,801 observations on MRO orbits 829–77,379 acquired between September 30, 2006 and January 28, 2023. Poleward of ~75–80° latitude in each hemisphere, coverage approaches 100% at this scale. Map shows all longitudes (180°W to 180°E) between 87.5°S and 87.5°N (limits imposed by MRO's orbital inclination). To take full advantage of three-dimensional processing methods, finer resolution at ≤0.5 km is desired. Global coverage at that resolution is 8%. (For interpretation of the references to colour in this figure legend, the reader is referred to the web version of this article.)

ratio of dielectric constants. This effect translates to *nominal* subsurface resolutions of ~5–10 m, depending on the material properties, with typical dielectric constants ranging from 2 for carbon dioxide ice to 9 for dense basalts. See however the discussion of the *effective* resolutions after processing in §2.2 below.

The SHARAD antenna emits a signal with a peak power of 10 W, which was projected to yield a postprocessing signal-to-noise ratio (S/N) at the surface as high as 58 dB (Seu et al., 2007b). In practice, data collected over the course of the mission on the nightside (when ionospheric effects are negligible) typically has maximum S/N values for the surface of about 40 dB. The positions of the MRO solar arrays (SA) and the high-gain antenna (HGA) have a strong impact on the total gain of the radar, such that a poor configuration can have 4 dB lower S/N than a more favorable SA-HGA configuration (Campbell et al., 2021a).

Because of practical limitations imposed by the necessary placement of imaging instruments on MRO's nadir deck, the SHARAD antenna was mounted in a non-optimal position on a corner of the zenith deck. To partly compensate for this deployment limitation, the MRO Project has been regularly executing roll maneuvers of up to 28° since early in the mission to reduce impacts on the SHARAD signals from the spacecraft body, and the solar arrays are stowed in a SHARAD-preferred orientation during nightside observations. These moderate rolls result in an average S/N improvement of 6 dB over that obtained with a nadir-pointing 0° roll angle (Campbell et al., 2021a). In contrast to their effect on the imaging instruments, the spacecraft rolls (which occur around the spacecraft velocity vector) do not cause a cross-track translation of SHARAD coverage at the surface—that is, the majority of the returned signal continues to occur from the nadir ground track for flat-lying surfaces due to the broad radiation pattern of the antenna. Recent updates to electromagnetic modeling of the effects of the spacecraft and its components on SHARAD signals indicate that another 5–10 dB of S/N improvement is achievable with roll angles in the range of 90–150° (DiCarlofelice et al., 2023). This result promises to dramatically improve SHARAD's capability to boost faint subsurface returns and enable the signal to detect dielectric contrasts at depths previously not achieved. The MRO Project and SHARAD team conducted a test of this very-large roll capability on May 2, 2023 using a roll angle of 120°. The results of the test achieved about 9 dB of S/N improvement as predicted by previous modeling efforts (DiCarlofelice et al., 2023). The teams are planning further use of this observing mode for high-value science targets.

Radar signals return from surface and subsurface interfaces to the MRO spacecraft at roughly the same interval as they are emitted by the antenna (i.e., every 1428 μs), but the delay between signal emission and reception varies with the spacecraft altitude and surface topography. Thus, the start time for a 135-μs receive window is adjusted to ensure the surface and subsurface returns are captured within that window. In addition, the along-track sampling interval of ~5 m is much finer than the nominal ~300 m resolution afforded by synthetic-aperture processing (Seu et al., 2007b), and thus the SHARAD team often takes advantage of onboard presumming to reduce the downlink data volume required by each observation, thereby enabling the collection of a greater number of observations. The onboard presumming factor typically does not exceed 8, which has a minimal impact on the resolution of surface features (Perry et al., 2023).

2.2. 2D processing methods

Prior to MRO's arrival at Mars, work began to develop processing algorithms aimed at decoding the downlinked data and transforming them into products that could be used to assess the properties of Martian surface and subsurface materials. The Italian SHARAD team developed software to produce the primary archival products for delivery to NASA's Planetary Data System (PDS) that are known as Experiment Data Records (EDRs) (Orosei, 2006a) and Reduced Data Records (RDRs) (Orosei, 2006b), where the former consist of "raw" observations in their least-processed form and the latter consist of two-dimensional (2D)

radargrams, wherein observations have been processed to produce profile images showing the returned radar power with delay time on the vertical axis and along-track distance on the horizontal axis (Fig. 2). These processing codes, which were developed prior to the mission in conjunction with industry partners and not made open source, were intended to be applied to all data with largely the same set of processing parameters so as to have a uniform set of products delivered to the PDS archive.

Given the expected variability of the scale of science targets, the U.S. SHARAD team foresaw a need for and began developing alternative processing methods that included the ability to customize processing parameters. This led Roger Phillips, SHARAD's original U.S. and Deputy Team Leader (DTL), to establish the Washington University Shallow Radar Processing System (WU-SHARPS), which was later renamed the Colorado Shallow Radar Processing System (CO-SHARPS) upon Phillips' relocation in 2007. CO-SHARPS offers a parameterized data processing service with access to two separate processing codes developed by the Jet Propulsion Laboratory (JPL) and the Smithsonian Institution (SI), internally referred to as the "QDA[1]" and "FPB[2]" processors. Given differences in parameters and the widespread use of the SI products, in 2013 the team chose to begin delivery of a set of products from the SI processor as supplemental PDS RDRs (Campbell and Phillips, 2014). In recent years, the SI processor underwent a major revision to improve correction of ionospheric effects, which has resulted in a new version of US SI PDS products (Campbell and Phillips, 2021). No plans currently exist for delivering JPL processor products to the PDS, but use of both processors is freely available through the CO-SHARPS interface (see http s://sharad.psi.edu/).

Each set of PDS products is accompanied by documentation and other files describing acquisition parameter settings, data processing procedures and parameters, location information, and other ancillary data. The PDS documentation provides complete descriptions of the methods used to produce each set of data products (Orosei, 2006a, 2006b; Campbell and Phillips, 2014). To summarize, the EDRs contain data as returned from the instrument, including any onboard coherent presumming but with no other signal processing applied. Since there is no application of range compression (i.e., deconvolution of the transmitted chirp), EDR data provide no obvious indication of subsurface interfaces and are thus not intended for direct geometric analysis. The RDR products are intended for geometric analysis, and the ground processing consists of decompression of onboard sample scaling, application of additional coherent presumming, range compression using either ideal or calibrated chirps (where the latter account for signal distortions due to temperature variations), application of a windowing function to reduce sidelobe effects, synthetic-aperture processing to improve along-track resolution and partially mitigate clutter (see §2.3), correction of phase distortion and delay induced by passage of the signal through the ionosphere, and removal of timing differences due to changes in the receive window, which follow altitude variations along the spacecraft ground track. Gain variation corrections for spacecraft altitude, roll angle, and the orientations of the solar array and high-gain antenna are not currently implemented in the JPL and SI processors, but

---

[1] The QDA processor is the successor to a prior one known as Focused Processor A (FPA), and both versions were developed by Ali Safaeinili at JPL. Upon installation at CO-SHARPS, the "QDA" acronym was attached to output products to distinguish them from FPA products. Safaeinili later stated that he never intended for this name to be applied to the processor or its outputs, which completely replaced the FPA products. Safaeinili never explained the QDA acronym, and its origin will remain a mystery due to his untimely death in 2009. One theory is that QDA stands for "Quick & Dirty processor A".

[2] The FPB acronym stands for "Focused Processor B", the development of which was led by Bruce Campbell at SI. This processor's development was preceded by that of "Unfocused Processor B (UPB)", which remains in use at CO-SHARPS for creating unfocused radargrams as well as ground-track maps and other ancillary products.
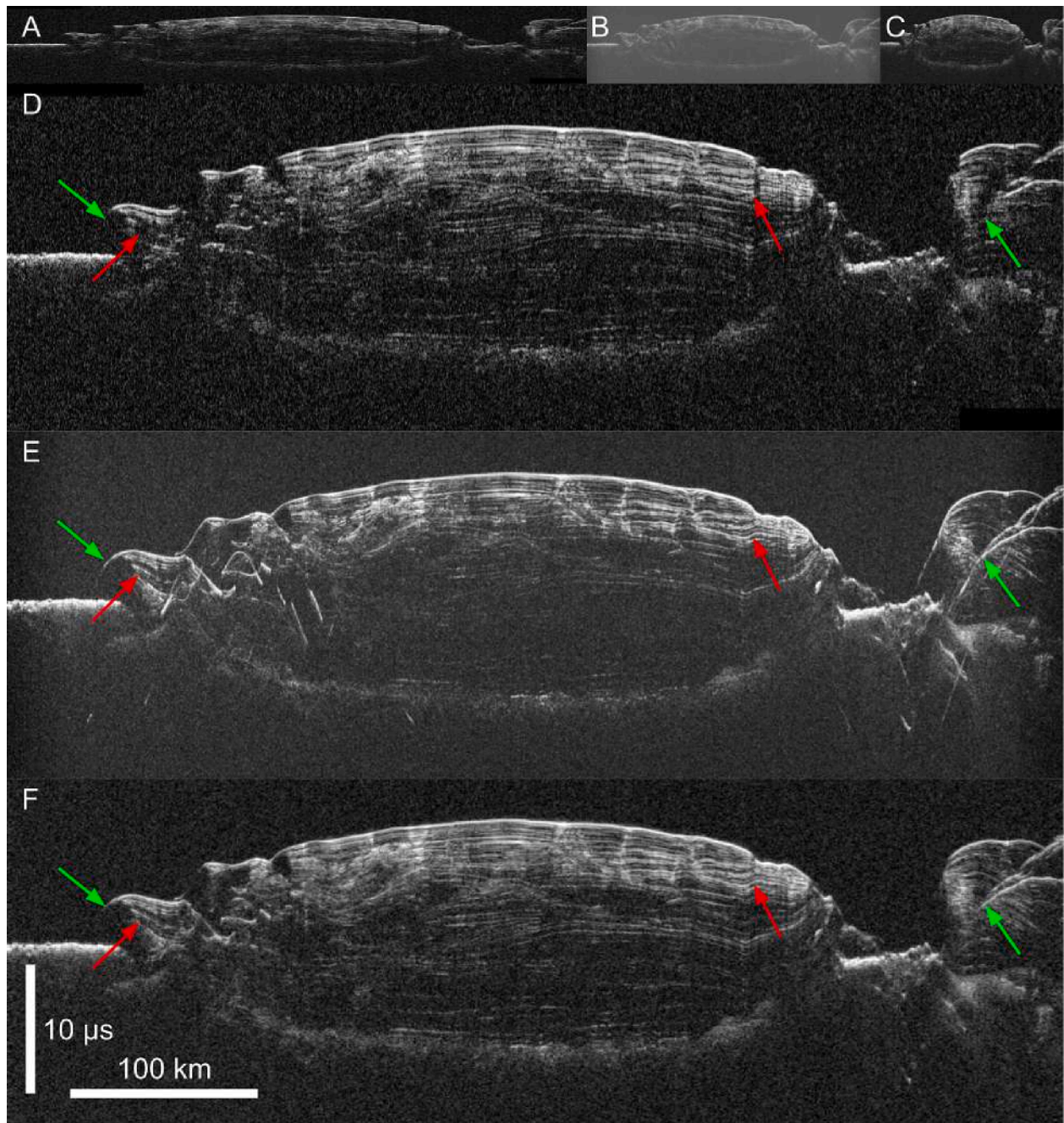
Fig. 2. Radargrams for SHARAD observation 04420–01 crossing the Gemina Lingula lobe of Planum Boreum. Panels A, B, and C are browse images from the Italian, US JPL, and US SI processors, respectively, that have been cropped in delay time but not otherwise modified to show differences in aspect ratio and power scaling. Panels D, E, and F are the same browse images as in A, B, and C, respectively, modified to matching sizes and scales to facilitate comparison of features. The shorter synthetic aperture of the Italian processor more effectively mitigates along-track clutter (at green arrows) while also suppressing some steeply dipping reflectors (at red arrows). (For interpretation of the references to colour in this figure legend, the reader is referred to the web version of this article.)

Table 1
Comparison of Italian and U.S. Radargram Processor Parameters.

Processor	Along-track sampling (m)	Range sampling[1] (ns)	Datum	Focusing aperture (s)	Number of Looks	Ionospheric correction method	Chirp envelope
Italian RDR	300	75.0	Spheroid	1–2	1	Phase-gradient autofocus	Ground calibration
US SI RDR	463	37.5	Areoid	8.77	7	Empirically derived function	Uniform with frequency
US JPL RDR	400	37.5	Spheroid	46.8	13	Chapman function	Uniform with frequency

[1] Italian RDR samples are complex whereas US RDR samples are real (no phase information).

the necessary math for that purpose is presented by Campbell et al. (2021a). Suppression of electromagnetic interference (EMI) is implemented in the SI processor, but the effectiveness depends strongly upon the nature and time variability of the EMI spectrum.

There are significant differences in the methods and parameters that each processor uses (Table 1). For example, along-track and range sampling differences result in different aspect ratios for the radargrams (Fig. 2A-C), and the choice of datum will determine whether the apparent slopes of reflecting interfaces are relative to the planetary shape or to an equipotential surface. While each focusing processor applies synthetic-aperture processing, the aperture lengths differ significantly, trading reduction of the along-track component of clutter against the imaging of steeper slopes. Each processor also uses a different empirical approach to mitigating phase distortion and delay introduced by the ionosphere.

Specialized techniques can be applied for certain situations, in addition to the standard processing. For example, to analyze frequency dependence of radar loss properties and layering geometries, SHARAD's bandwidth can be computationally subdivided through the use of so-called "split-chirp" processing (Campbell and Morgan, 2018). Bandwidth extrapolation techniques can also be employed to enhance vertical resolution (Raguso et al., 2018). In cases where ground tracks are closely spaced, coherent summing can be exploited to improve the signal-to-noise ratio and reduce off-nadir clutter (Mastrogiuseppe et al., 2019). See also Raguso et al. (2023).

As is often reported in the literature, SHARAD has a 15-m freespace range (vertical) resolution and a subsurface resolution improvement to ~5–10 m (depending on the material properties, with typical dielectric constants ranging from 2 for carbon dioxide ice to 9 for dense basalts). However, these resolutions are generally not realized because of the processing used to produce the 2D radargrams wherein a frequency-domain tapering function (often referred to as windowing and defaulted to a Hann filter for the three processors) is applied to the data as a means to suppress sidelobes (an undesirable ringing effect in the range direction of the returned signals centered on interfaces of high dielectric contrast, most notably at the surface). This windowing effectively broadens the range-compressed impulse response by a factor of ~2 (Cumming and Wong, 2005, §3.3.4). In practice, the effective subsurface resolution for SHARAD radargrams are thus ~10–20 m.

2.3. Clutter and simulations

Over flat-lying surfaces, SHARAD echoes are predominantly returned from nadir, but nearby off-nadir surface topography and subsurface structures may produce returns, referred to as clutter, that arrive at the same time as nadir surface and subsurface returns, causing a potential for misinterpretation. Over sloping surfaces, SHARAD echoes are predominantly returned from locations on the surface that are orthogonal to the propagation direction of the signal coming from the spacecraft, and such locations may be fore, aft, or cross-track relative to the nadir point, depending on the orientation of the surface slope. To aid the interpretation of radargrams, surface-clutter simulations may be produced for areas where digital elevation models (DEMs) are available. To the extent that the DEM captures the true topography and the simulator reproduces the actual radar characteristics, the resulting cluttergram (i.e., simulated radargram) will reproduce both nadir and off-nadir returns from the surface at the same along-track locations and delay times as in the actual radargram. A visual comparison of the cluttergram and radargram will then allow one to distinguish true subsurface returns from surface clutter. Subsurface clutter is not often simulated, and would require foreknowledge of subsurface interfaces and material properties. Simulators can also be configured to map the echo source locations, such as for the first returns from the surface along the spacecraft trajectory. Clutter simulators have been developed by SHARAD team members at the University of Texas (UT) and at the University of Arizona (UA) that correspond, respectively, to JPL and SI

radargrams, and the UA versions are available in the PDS (Choudhary et al., 2016; Christoffersen et al., 2021). Note that these simulators are aimed at predicting the arrival of radar reflections in time and space, but they do not attempt to fully reproduce their expected amplitude or power. Fig. 3 presents an example of a cluttergram and corresponding map of surface echo power for the same SHARAD observation as that presented in Fig. 2.

2.4. 3D processing methods

While the along-track component of clutter is largely mitigated by the synthetic-aperture focusing applied in the 2D processors, the cross-track component largely remains, and thus 2D radargrams contain substantial geometric distortions and signal interference that can only be partially addressed through the use of surface-clutter simulator outputs. In areas where dense coverage from many orbital passes has been obtained, it is possible to apply three-dimensional (3D) radar processing methods. To the extent that clutter sources are sufficiently sampled by the set of observations (which leads directly to a choice of synthetic-aperture processing parameters), 3D imaging techniques may be used to restore clutter signals to their points of origin in 3D space, thereby greatly clarifying the representation of surface and subsurface structures (Foss et al., 2023). Such methods have been developed extensively over many decades for both seismic and radar sounding data in terrestrial investigations, and beginning in 2010 these techniques were adapted for use with SHARAD data. To date, this process has been carried out for both polar regions (Foss et al., 2017; Putzig et al., 2018, 2022) and for a portion of Deuteronilus Mensae that contains widespread debris-covered glaciers (Perry et al., 2023). Work is underway to expand the application of 3D processing for other mid-latitude locations where coverage is sufficiently dense. Results thus far indicate that a ground-track spacing at the nominal ~3-km resolution established by the signal's Fresnel zone at the surface is more than adequate to produce good imaging results, but finer-scale ground-track spacing down to the along-track resolution of input radargrams (typically 0.3 to 0.5 km) can significantly improve the imaging of fine-scale structures (Perry et al., 2023).

2.5. Dielectric constant and loss estimation

SHARAD data can be used to estimate the dielectric properties of the subsurface, which in turn can constrain the composition of the shallow Martian crust over probing depths of the instrument (10s to 1000s of meters, depending on the nature of the substrate). For electromagnetic waves, the real part of dielectric permittivity (ε') is related to the density and porosity of the medium. Given the low density of volatile ices, estimating ε' provides a means to differentiate ice-rich materials from those containing higher fractions of lithic material. Water ice under Martian temperatures exhibits an ε' of ~3.0–3.2 (see Grima et al. (2009) and references therein) and other radar studies of the PLDs and mid-latitude glaciers have returned estimates close to this value (e.g., Putzig et al., 2009; Holt et al., 2008). On the other end of the Martian geologic spectrum, basaltic lava flows—which constitute the source of lithic materials within the Martian regolith—have been found to exhibit ε' values >7 (e.g., Carter et al., 2009a).

Changes in the wavelength of radar signals as they move through the subsurface are determined by the dielectric permittivity of the substrate. One way to estimate ε' is by measuring the fluctuations in the speed of light as it travels through the subsurface. However, to accomplish this measurement using SHARAD data, it is necessary to have independent knowledge of the depth of an interface associated with a subsurface reflection or to make a reasonable assumption about it. In cases where the source of a subsurface reflection is interpreted to be the base of a stratigraphically younger deposit elevated relative to the surrounding, older Martian surface, it is possible to estimate the thickness of the deposit by extrapolating the elevation of the older surface (via the use of
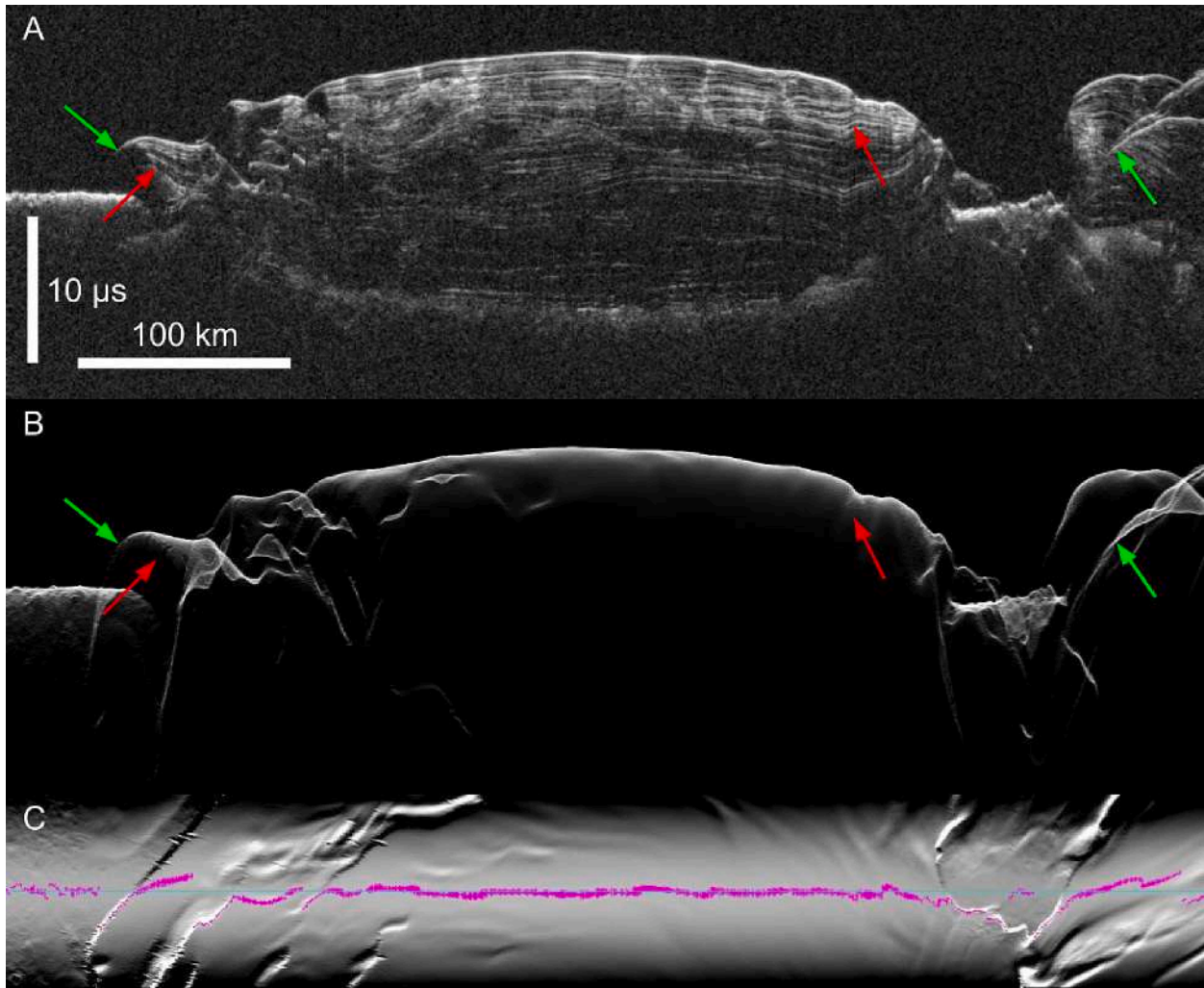
Fig. 3. Panel A presents the same US SI PDS radargram, for SHARAD observation 04420–01, as that in Fig. 2F. Panel B presents a corresponding UA PDS cluttergram and Panel C presents a corresponding map of the surface echo power predicted by the simulator, which uses a MOLA 128-pixel-per-degree DEM. Returns seen in both the radargram and cluttergram (e.g., at green arrows) can be attributed to surface features whereas returns subsequent to the first returns in the radargram that do not have corresponding returns in the cluttergram may be attributed to subsurface features, assuming the DEM is sufficiently representative of the true surface (e.g., at red arrows). Magenta pixels in Panel C denote the location of first returns in the cluttergram, which can deviate significantly from the nadir track (cyan line) of the observation, depending on nearby surface structures. The echo-power map closely resembles a shaded-relief elevation map. (For interpretation of the references to colour in this figure legend, the reader is referred to the web version of this article.)

DEMs derived from elevation data or stereo images). Using the time delay between surface and subsurface reflections as recorded by SHARAD and such thickness measurements, one can invert for ε'. This methodology has been used widely and applied to a range of landforms from glacial deposits (e.g., Holt et al., 2008) to lava flows (e.g. Carter et al., 2009a).

Taking an alternative approach, Phillips et al. (2011) were able to establish that extensive zones of unusually low radar reflectivity present in Australe Mensa atop the south polar layered deposits (SPLD) are composed of carbon dioxide ice by assuming that undulations in otherwise horizontal layers, which underlie the carbon dioxide ice layers, are distortions caused by variations in lightspeed rather than true structural relief. Carbon dioxide ice under Martian conditions has an ε' of $\sim$2, which locally decreases the time delay to the underlying reflections relative to those of the surrounding SPLD that is composed of water ice.

The imaginary part of dielectric permittivity (ε'') is strongly modulated by the mineralogy of the substrate material and affects the attenuation, or loss of signal strength experienced by a radar signal propagating through the subsurface. The ratio of the two components ($\varepsilon'/\varepsilon''$) is termed the loss tangent (tanδ), and provides an additional avenue to explore subsurface composition. In particular, thoroughly frozen, pure ices are characterized by extremely low values of tanδ, and estimates of the massive ices in PLD and mid-latitude glacier deposits have yielded values of tanδ <0.003 (Picardi et al., 2005; Plaut et al., 2007; Grima et al., 2009; Campbell and Morgan, 2018). Martian lava flows exhibit tanδ values that are an order of magnitude greater, up to 0.022 (Carter et al., 2009a; Campbell and Morgan, 2018), and even increased concentrations of dusty layers within the north polar layered deposits (NPLD) have been found to significantly increase tanδ to values >0.003 (Grima et al., 2009).

Multiple approaches have been applied to estimate the tanδ of Martian materials using SHARAD data. In the case of dipping subsurface reflectors, the rate of change of the ratio of the subsurface-to-surface power return with increased time delay can be used to constrain tanδ (Campbell et al., 2008). This technique requires some assumptions, for instance that the surface roughness be comparable to that of the basal interface at the SHARAD wavelength, a condition that is sometimes unmet for smooth, dusty regions that cover rough lavas. The bandwidth of the SHARAD chirp can also be leveraged to constrain tanδ. By splitting

the chirp into high and low frequency channels, the relative power of subsurface returns can be compared between these channels to estimate the tanδ of the overlying material (Campbell and Morgan, 2018).

3. Results and discussion

3.1. Polar science

SHARAD has been especially effective in sounding of the Martian polar caps, whose cold temperatures and low lithic content often allow signals to penetrate through 2–3 km of icy layers, with enough dielectric contrast to provide reflections from up to 48 interfaces at depth (Seu et al., 2007a; Putzig et al., 2009). Here, we summarize results for both polar regions.

3.1.1. Planum Boreum

In the north, internal layering is relatively uniform over the thickness of the NPLD, which extends to depths of up to 2 km. Zones of high reflectivity alternate with zones of lower reflectivity (Phillips et al., 2008; Putzig et al., 2009), and low signal loss provides a strong argument for the purity of the ice (<~5% lithics) (Grima et al., 2009). In Planum Boreum's main lobe, the NPLD sits atop a zone of diffuse reflectivity with no distinct basal return that corresponds to the basal cavi and rupēs units (Tanaka and Fortezzo, 2012; Brothers et al., 2015; Nerozzi and Holt, 2018) whereas in much of the Gemina Lingula lobe, the NPLD appears to sit directly atop Vastitas Borealis units. A dramatic early finding is that the load of Planum Boreum materials has induced little to no lithostatic compensation, implying lower than expected heat flow and a thicker than expected lithosphere, at least in the north polar region (Phillips et al., 2008). While SHARAD's ~ 15-m vertical resolution hampers efforts to relate radar reflections to the finer-scale layering seen in visible imagery (Christian et al., 2013), intensive mapping efforts have revealed a host of internal features, including a buried chasma (Holt et al., 2010), trough-bounding surfaces extending through the upper half of the NPLD (Smith and Holt, 2010, 2015), and a surface-conformal sequence at the top of the NPLD deposited after the most recent Martian ice age (Smith et al., 2016; Putzig et al., 2022). An improved understanding of subsurface structures and the variability of dust content within the ice has been achieved through a combination of modeling of the radar response to different stratigraphies (Lalich et al., 2019; Courville et al., 2021) and advanced processing techniques, such as 3D radar imaging (§2.4; Putzig et al., 2018, 2022) (Fig. 4), incoherent summation (Putzig et al., 2022), superresolution (Raguso et al., 2018), and subband processing (Campbell and Morgan, 2018; Jawin et al., 2022).
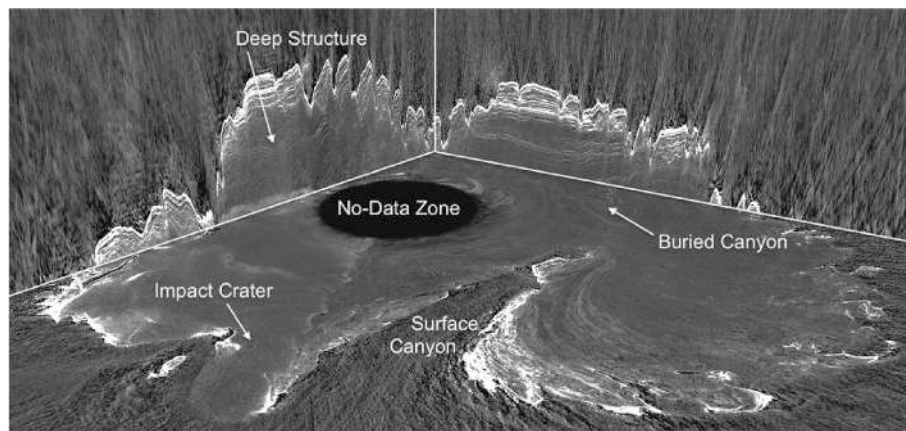
3.1.2. Planum Australe

In the south, the signal penetration depth and continuity of radar interfaces across the SPLD is much more variable than in the north (Seu et al., 2007a; Phillips et al., 2011; Whitten and Campbell, 2018). Depositional patterns are absent or more difficult to interpret at the SPLD outside of a depocenter near the highest elevation (Whitten et al., 2017) and for some recent activity near the spiral troughs (Smith et al., 2015). Near the pole in Australe Mensa, SHARAD revealed a near-surface deposit containing up to three units of massive carbon dioxide ice with little to no internal radar reflectivity separated by thin layers of water ice (Phillips et al., 2011; Putzig et al., 2018; Alwarda and Smith, 2021) (Fig. 5). The carbon dioxide ice contains sufficient mass to more than double atmospheric pressure if sublimated, which was likely the case prior to 510 ka (Bierson et al., 2016; Buhler, 2023; Buhler et al., 2019).

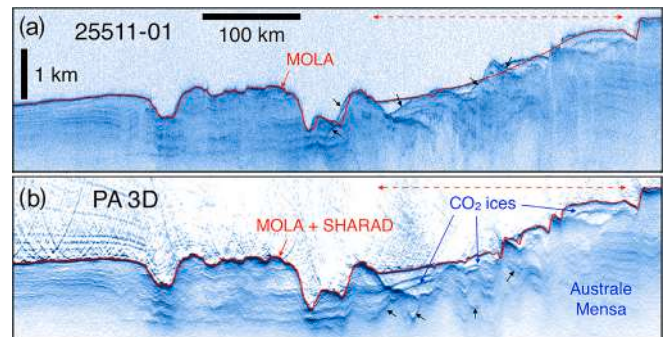Other zones of low reflectivity occur elsewhere in the SPLD, but they

Fig. 5. Excerpt from Fig. 4 of Putzig et al. (2018), showing SHARAD depth profiles for (a) observation 25511–01 and for (b) data from the Planum Australe 3D radargram extracted for the same ground track that extends across Ultima Lingula and the carbon dioxide ices in paleo-troughs on the edge of Australe Mensa. The 3D imaging process correctly positions surface and subsurface features, separating interfering nadir and off-nadir returns in the 2D profile, and enhancing S/N at depth, albeit with some loss of vertical resolution in this case. Black arrows in (a) indicate examples of clutter signals largely corrected by 3D processing. Black arrows in (b) indicate examples of likely artifacts in the 3D radargram due to incomplete correction of off-nadir echoes from features with inadequate SHARAD coverage. Red lines are the MOLA-derived surface profile along the ground track, replaced by the SHARAD-derived surface in (b) in the zones indicated by the red dashed arrow where SHARAD observes higher latitudes than MOLA did. Depth conversion assumes pure water ice ($\varepsilon' = 3.15$), which does not remove the distortions where CO_2 is present as first identified by Phillips et al. (2011). (For interpretation of the references to colour in this figure legend, the reader is referred to the web version of this article.)

Fig. 4. Perspective view of the interior of Planum Boreum from 3D radar imaging, showing orthogonal vertical profiles through ≤ 2 km of NPLD and a horizontal slice across Gemina Lingula (right) and the main lobe. No-data zone is 300 km across (vertical exaggeration is 100:1). After Fig. 1 of Putzig et al. (2022).

have not been shown to contain carbon dioxide ice, and areas of diffuse radar returns (often referred to as "radar fog") permeate restricted zones in some areas and the entire stack of layers in others (Phillips et al., 2011; Whitten and Campbell, 2018). Surprisingly, the fog effect does not appear to be associated with a strong attenuation of the radar signal (Abu Hashmeh et al., 2022), in contrast to the similarly diffuse echoes in the basal units of Planum Boreum.

3.2. Non-polar cryosphere

The periphery of many high-standing massifs and mesas in the mid-latitudes of Mars have long been known to contain apparent viscous-flow features, termed lobate debris aprons (LDAs) (Squyres, 1979), but their ice content was not well constrained prior to the arrival of SHARAD. Radar soundings of LDAs often obtain strong basal returns and exhibit low loss tangents, demonstrating that the features are actually ice-rich debris-covered glaciers (Holt et al., 2008; Plaut et al., 2009). Further investigations of LDAs at Neredium Montes (Berman et al., 2021) and Phlegra Montes (Gallagher et al., 2021) included SHARAD analyses that found similar results of hundreds of meters of pure ice covered by a 4–7 m debris layer. Surface roughness and interference from clutter signals often prevent or obfuscate the basal returns at LDAs (Petersen et al., 2018), but the latter effect can be addressed with 3D radar imaging, given sufficient coverage (Perry et al., 2023).

Beyond the LDAs, SHARAD also penetrates icy materials associated with pedestal craters (Nunes et al., 2011) and obtains weaker reflections from what appears to be the base of ground ices in an isolated area around the Phoenix landing site (Putzig et al., 2014) as well as in more extensive regions within Arcadia Planitia (Bramson et al., 2015; Ramsdale et al., 2017) and Utopia Planitia (Stuurman et al., 2016; Séjourné et al., 2019). Smaller ground-ice deposits have been investigated by SHARAD in the southern hemisphere, but the results were ambiguous (Adeli et al., 2019).

While the mid-latitude ices are of high scientific interest due to their connection to climate cycles on Mars, there have also been some efforts to better map their extent and nature with a view toward using the ice as a resource to sustain human missions, including the provision of fuel through reaction with atmospheric carbon dioxide for ground operations and Earth-return vehicles. To that end, NASA has funded efforts to map these mid-latitude ices in areas where the first human landing sites may be considered (Morgan et al., 2021; Putzig and Morgan et al., 2023). The Mars Subsurface Water Ice Mapping (SWIM) project combines results derived from SHARAD surface and subsurface reflections together with neutron and thermal spectrometer data and geomorphologic data to assess the consistency of all of these datasets with the presence of subsurface ice across the Martian mid-latitudes (Fig. 6). These results are intended to inform the planning of future missions, both to acquire new types of data that better inform the depth to and nature of the buried ice and to carry out advance reconnaissance for human landing sites.

3.3. Non-icy terrains

SHARAD subsurface detections are not restricted to volatile-rich terrains. Successful sounding has been applied across the full range of Martian material types from sedimentary units to volcanic bedrock. Attenuation of SHARAD signals is largely a function of substrate density and mineralogy, so coherent, mafic lava flows restrict penetration depth of the signal to at least an order of magnitude less than is typically achieved within the PLDs. Nevertheless, SHARAD has supported several detailed studies of volcanic stratigraphy. Stacks of at least five lava flows have been mapped in the youngest volcanic province of Elysium Planitia (Morgan et al., 2015) (Fig. 7). Tracing out such subsurface structure has enabled the possible eruption sources to be identified in addition to providing a means of reconstructing the preexisting terrain. Volcanic flows have embayed several late Amazonian outflow channels within
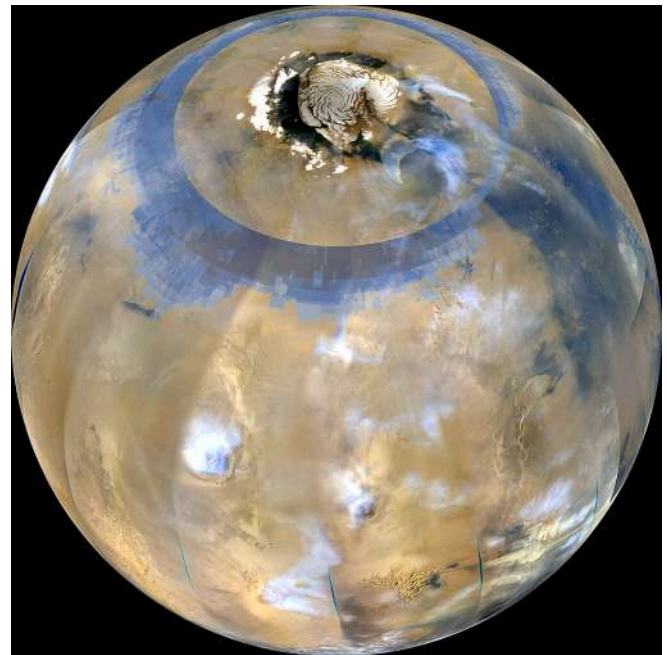

Fig. 6. Global view of Mars in a MRO Mars Color Imager mosaic overlain in blue shades with regions in the northern hemisphere of high consistency with the presence of near-surface ice in neutron and thermal spectrometer data, geomorphic feature mapping, and surface and subsurface radar analysis. Journal cover image from Morgan et al. (2021). (For interpretation of the references to colour in this figure legend, the reader is referred to the web version of this article.)

the Elysium region. SHARAD detections of the base of such flows as well as layering within the older volcanic units that were incised by the channels have enabled the original morphology and channel characteristics to be constrained, shedding light on possible interaction of volcanics and groundwater (Morgan et al., 2013). Beyond Elysium Planitia, the base of lava flows have been identified within all other Amazonian volcanic terrains, including the calderas of shield volcanoes (Ganesh et al., 2020), and positive detections have also been made within limited regions of Hesperian volcanic terrain (Bharti et al., 2022).

The majority of Martian volcanic provinces are blanketed with dust deposits (Ruff and Christensen, 2002). The homogeneous spectral nature of Martian dust has made assessments of the composition of volcanic terrain challenging, especially in comparison to equivalent lunar volcanic studies. Through the application of SHARAD-based dielectric property estimation techniques (see §2.5) of Martian volcanic units, new constraints on the material properties of individual flows have been made. A significant portion of this research has focused on the Tharsis region, where prominent lava flow fields with thicknesses ranging from 20 to 60 m have been identified. These fields have been found to demonstrate a variety of ε' values, ranging from 7 to over 10, as well as loss tangents between 0.01 and 0.08 (Carter et al., 2009a; Shoemaker et al., 2022; Simon et al., 2014). The observed variations in dielectric properties suggest the presence of different igneous compositions, possibly including varying levels of high-loss minerals (Shoemaker et al., 2022). Interestingly, the accumulation of dust across the Tharsis region appears to aid subsurface detections by reducing the impedance contrast at the surface, which allows more signal to enter the subsurface (Carter et al., 2009a; Shoemaker et al., 2022).

SHARAD data have proved valuable in studying sedimentary units on Mars deposited during each of the Noachian, Hesperian, and Amazonian epochs, and derived from a range of geological processes. As described above in regards to lava flow units, SHARAD investigations of sedimentary deposits have provided valuable insights into their dielectric properties and associated stratigraphy. Such studies enable
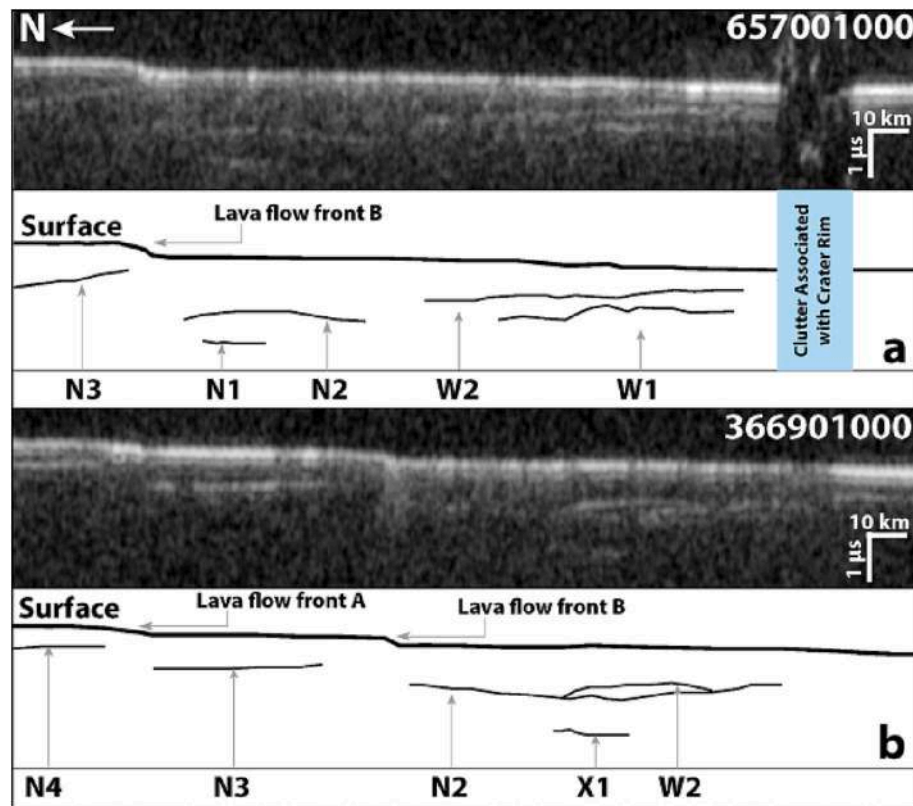
Fig. 7. Examples of SHARAD radargrams with corresponding sketch maps showing (a and b) stacks of reflectors in the central Elysium volcanic province. From Fig. 2 of Morgan et al. (2015).

reconstruction of local depositional histories and shed light on the geological processes responsible for sedimentary formations. Together with other datasets, SHARAD investigations have explored the infilling of the ancient lowland surface of Amazonis Planitia (Campbell et al., 2008), surface clays in Eastern Valles Marineris (Rezza, 2021), and the possible reworking of ash deposits surrounding Valles Marineris (Mishev and Smith, 2022).

One of the most substantial, and certainly the most enigmatic sedimentary deposits is the Medusae Fossae Formation (MFF). Extending around a quarter of Mars' circumference along the equator, the MFF represents tens of meters to kilometers thick accumulations of layered material. Interpreted to be Hesperian or older in age (Kerber and Head, 2012, 2010; Zimbelman and Scheidt, 2012), the origin of the deposits has been a subject of debate for decades. Based on morphologic similarities with the PLDs, Schultz and Lutz (1988) suggested that the MFF represents the remnants of a paleo-polar deposit. Alternatively, many authors have argued the MFF are a product of explosive volcanic eruptions (Bradley et al., 2002; Hynek et al., 2003; Kerber et al., 2011; Zimbelman and Griffin, 2010; Mouginis-Mark and Zimbelman, 2020). MARSIS soundings over the prominent MFF deposits reveal a bulk ε' of ~3, suggesting either thick accumulations of unconsolidated sediments or a high ice content (Watters et al., 2007).

SHARAD only detects a basal reflector within limited regions of the MFF, as the radar signal is attenuated relative to MARSIS over the thickest sections of the deposits. Where basal reflectors can be leveraged with SHARAD data to estimate the dielectric properties, bulk ε' values of 2–3 have been estimated (Carter et al., 2009b; Morgan et al., 2015) (Fig. 8). Evaluations of loss estimates over the upper ~300 m (where SHARAD detects the basal reflector) suggest an increase in density with depth, supporting the presence of a self-compacting dry material (Campbell et al., 2021b). To reconcile the MARSIS bulk ε' estimates with the near-surface SHARAD conclusions requires that the MFF be a hybrid deposit with dry sediments emplaced (possibly through ash eruptions)

over a minimally compacting, low-loss material such as ice (Campbell et al., 2021b).

3.4. Surface roughness and density

SHARAD sounding data generally include first returns from the surface interface, and the strength of the peak echo and its decline with increasing delay correlate with the density and roughness of the surface at the horizontal scale of the radar wavelength. For SHARAD, this means decameter lateral scales (Campbell et al., 2013), between those of MOLA's > 300-m baseline and meter-scale pulse-width roughness metrics (Kreslavsky and Head, 2000; Neumann et al., 2003). Roughness and density studies provide new constraints on surface characteristics important to landing-site safety and trafficability (Putzig et al., 2017). The ability to assess near-surface density also contributes to understanding the physical properties of terrain in a broad range of geologic settings (Grima et al., 2012, 2022; Campbell et al., 2013; Morgan et al., 2021).

3.5. Ionosphere studies

In addition to surface and subsurface sounding, SHARAD measurements of the ionosphere's total electron content (TEC) provide a unique, long-term record of interactions with the solar wind and the remanent magnetic field. The TEC value at each ~35 km footprint for dayside observations comes from the phase distortion term estimated by the radargram autofocusing process, which in turn was found to correlate with the radar-echo time delay offset and thus the TEC (Campbell et al., 2011, 2021a). A relationship of the TEC temporal variations to solar zenith angle and solar flux is in keeping with photochemical equilibrium theory, and consistent spatial variations of the TEC also enable new mapping of crustal magnetic fields in Mars' southern hemisphere (Mendillo et al., 2017; Campbell and Morgan, 2023). The TEC data also
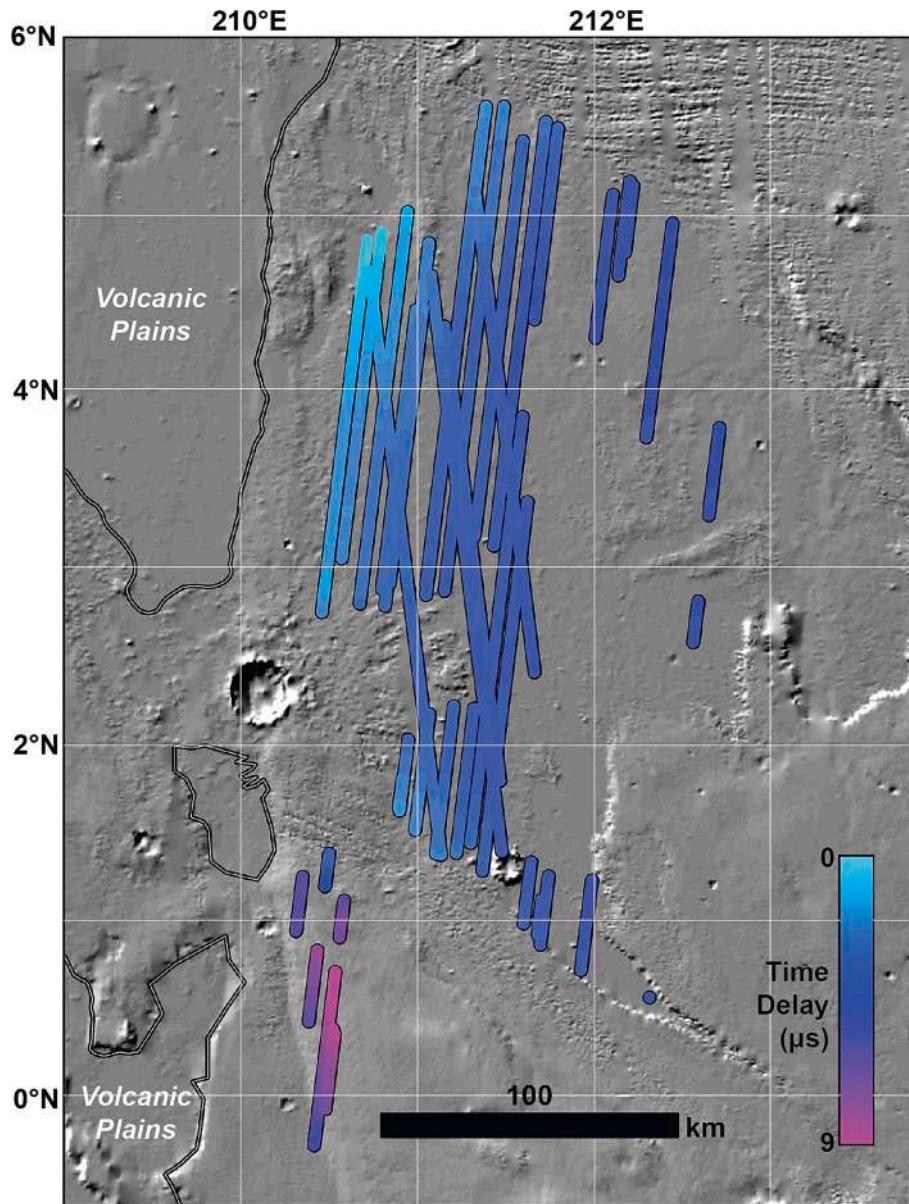
N.E. Putzig et al.

Fig. 8. Time delay of SHARAD detected basal reflections below the Amazonis region of the MFF (outlined in black). The deposits become progressively thicker away from the volcanic plains, though the basal reflector becomes undetectable beyond ~ 9 µs. Background is MOLA hillshade, SHARAD data adapted from Campbell et al. (2021b).

characterize specific events such as the passage of comet Siding Spring, where elevated TEC values point toward ablation of cometary dust as a source of a secondary layer of ions at Mars (Restano et al., 2015). In addition, the TEC observations show that coronal-mass-ejection events elevate ionization at lower altitudes and result in temporary blackouts, wherein surface and subsurface returns are drastically attenuated (Campbell et al., 2013; Lester et al., 2022).

3.6. Conclusions

SHARAD provides unique contributions to the understanding of Mars, extending from a major revision of lithospheric thickness and deep-interior heat flow to a new view of the spatial and temporal variability of the ionosphere. In between, SHARAD illuminates polar-cap layering, structure, and interior properties at a level of detail unparalleled even for the terrestrial case, enables the mapping and assessment of mid-latitude ices that inform Martian climate history and promise to supply critical resources for human explorers, and reveals the structure

and properties of non-icy terrains in a distinctive contribution to the record of volcanic and sedimentary processes.

SHARAD's contributions to the study of ice on Mars have been well received by the wider community. Among many important discoveries, these contributions identified climate signatures and explained features in the PLDs that were debated even as early as the Mariner 7 flyby in 1969. Since 2015, with the discovery of accessible ice in the mid-latitudes, the Mars Exploration Program, the National Academy of Science, and NASA have added priorities for better characterizing the location and quantity of that ice through the SWIM project and development of the International Mars Ice Mapper Mission in conjunction with Canada, Italy, Japan, and the Netherlands (I-MIM MDT, 2022). The utility of radar at Mars extends well beyond characterizing ice, as the geologic history is revealed in a third dimension, and an imaging synthetic-aperture radar like I-MIM would enable mapping of features buried by dust.

Many of the studies outlined above have resulted from the series of extended mission phases that have been awarded since the end of MRO's

primary science phase in 2008. In particular, the application of 3D processing techniques and the spatial reconstructions of the ionosphere have only been made possible due to a decade and a half of targeted data collection. Through this time, science application, data collection techniques, and subsequent processing have evolved significantly, and the scientific application of SHARAD is greater today than when MRO first arrived at Mars. The MRO spacecraft and the SHARAD instrument remain healthy and are capable of another decade or more of continued operations. To take full advantage of advanced processing techniques, increased coverage densities are needed in many regions. In addition, the potential for a dramatic improvement in signal quality and penetration depth afforded by targeted use of high-angle spacecraft rolls holds the promise of new discoveries in the years to come.

Contributions

Each author declares substantial contributions through the following:

(1) the conception and design of the study, or acquisition of data, or analysis and interpretation of data and (2) drafting the article or revising it critically for important intellectual content.

Putzig - SHARAD US & Deputy Team Leader; data acquisition and analysis & interpretation; manuscript drafting and editing.

Seu - SHARAD Team Leader; instrument conception & design, data acquisition, and analysis; manuscript review.

Morgan - SHARAD Co-Investigator; data acquisition and analysis & interpretation; manuscript drafting and editing.

Smith - SHARAD Co-Investigator; data acquisition and analysis & interpretation; manuscript drafting and editing.

Campbell - SHARAD Co-Investigator; instrument conception & design, data acquisition, and analysis & interpretation; manuscript drafting and editing.

Perry - SHARAD Team Member; data acquisition and analysis & interpretation; manuscript drafting and editing.

Mastrogiuseppe - SHARAD Co-Investigator; data acquisition and analysis & interpretation; manuscript review and editing.

Declaration of Competing Interest

The authors declare that they have no known competing financial interests or personal relationships that could have appeared to influence the work reported in this paper.

Data availability

SHARAD data are available on the Geosciences node of the Planetary Data System (PDS) at https://pds-geosciences.wustl.edu/missions/mro/sharad.htm. Additional information and products can be found on the SHARAD team website at https://sharad.psi.edu.

Acknowledgments

References

Abu Hashmeh, N., Whitten, J.L., Russell, A.T., Putzig, N.E., Campbell, B.A., 2022. Comparable bulk radar attenuation characteristics across both Martian polar layered deposits. J. Geophys. Res. Planets 127. https://doi.org/10.1029/2022JE007566.

Adeli, S., Hauber, E., Michael, G.G., Fawdon, P., Smith, I.B., Jaumann, R., 2019. Geomorphological evidence of localized stagnant ice deposits in Terra Cimmeria,

Mars. J. Geophys. Res. Planets 124, 1525–1541. https://doi.org/10.1029/2018JE005772.

Alwarda, R., Smith, I.B., 2021. Stratigraphy and volumes of the units within the massive carbon dioxide ice deposits of Mars. J. Geophys. Res. Planets 126. https://doi.org/10.1029/2020JE006767.

Berman, D.C., Chuang, F.C., Smith, I.B., Crown, D.A., 2021. Ice-rich landforms of the southern mid-latitudes of Mars: a case study in Nereidum Montes. Icarus 355, 114170. https://doi.org/10.1016/j.icarus.2020.114170.

Bharti, R.R., Smith, I.B., Mishra, S.K., Srivastava, N., Shukla, S.H., 2022. SHARAD detection of sedimentary infilling within an unnamed crater near Mangala Fossa region, Mars. Icarus 371, 114713. https://doi.org/10.1016/j.icarus.2021.114713.

Bierson, C.J., Phillips, R.J., Smith, I.B., Wood, S.E., Putzig, N.E., Nunes, D., Byrne, S., 2016. Stratigraphy and evolution of the buried CO_2 deposit in the Martian south polar cap. Geophys. Res. Lett. 43, 4172–4179. https://doi.org/10.1002/2016GL068457.

Bradley, B.A., Sakimoto, S.E.H., Frey, H., Zimbelman, J.R., 2002. Medusae fossae formation: new perspectives from Mars global surveyor. J. Geophys. Res. 107, 5058. https://doi.org/10.1029/2001JE001537.

Bramson, A.M., Byrne, S., Putzig, N.E., Sutton, S., Plaut, J.J., Brothers, T.C., Holt, J.W., 2015. Widespread excess ice in Arcadia Planitia, Mars. Geophys. Res. Lett. 42, 6566–6574. https://doi.org/10.1002/2015GL064844.

Brothers, T.C., Holt, J.W., Spiga, A., 2015. Planum Boreum basal unit topography, Mars: irregularities and insights from SHARAD. J. Geophys. Res. 120, 1357–1375. https://doi.org/10.1002/2015JE004830.

Buhler, P.B., 2023. A 510,000-year record of Mars' climate. Geophys. Res. Lett. 50 https://doi.org/10.1029/2022GL101752 e2022GL101752.

Buhler, P.B., Ingersoll, A.P., Piqueux, S., Ehlmann, B.L., Hayne, P.O., 2019. Coevolution of Mars's atmosphere and massive south polar CO_2 ice deposit. Nat. Astron. https://doi.org/10.1038/s41550-019-0976-8

Campbell, B.A., Morgan, G.A., 2018. Fine-scale layering of Mars polar deposits and signatures of ice content in non-polar material from multi-band SHARAD data processing. Geophys. Res. Lett. 45, 1759–1766. https://doi.org/10.1002/2017GL075844.

Campbell, B.A., Morgan, G.A., 2023. SHARAD observations of Mars dayside ionospheric patterns controlled by remnant magnetic fields. 54th Lunar Planet. Sci. Conf., Abs. 2254.

Campbell, B.A., Phillips, R.J., 2014. Mars Reconnaissance Orbiter Shallow Radar radargram data. NASA Planet. Data Syst. MRO-M-SHARAD-5-RADARGRAM-V1.0. https://doi.org/10.17189/1519527.

Campbell, B.A., Phillips, R.J., 2021. Mars Reconnaissance Orbiter Shallow Radar radargram data. NASA Planet. Data Syst. MRO-M-SHARAD-5-RADARGRAM-V2.0. https://doi.org/10.17189/YB1W-F075.

Campbell, B., Carter, L., Phillips, R., Plaut, J., Putzig, N., Safaeinili, A., Seu, R., Biccari, D., Egan, A., Orosei, R., 2008. SHARAD radar sounding of the Vastitas Borealis Formation in Amazonis Planitia. J. Geophys. Res. 113, E12010. https://doi.org/10.1029/2008JE003177.

Campbell, B.A., Putzig, N.E., Carter, L.M., Phillips, R.J., 2011. Autofocus correction of phase distortion effects on SHARAD echoes. IEEE Geosci. Remote Sens. Lett. 8, 939–942. https://doi.org/10.1109/LGRS.2011.2143692.

Campbell, B.A., Putzig, N.E., Carter, L.M., Morgan, G.A., Phillips, R.J., Plaut, J.J., 2013. Roughness and near-surface density of Mars from SHARAD radar echoes. J. Geophys. Res. 118, 436–450. https://doi.org/10.1002/jgre.20050.

Campbell, B.A., Putzig, N.E., Foss II, F.J., Phillips, R.J., 2014. SHARAD signal attenuation and delay offsets due to the Martian ionosphere. IEEE Geosci. Remote Sens. Lett. 11, 632–635. https://doi.org/10.1109/LGRS.2013.2273396.

Campbell, B.A., Morgan, G.A., Bernardini, F., Putzig, N.E., Nunes, D.C., Plaut, J.J., 2021a. Calibration of Mars Reconnaissance Orbiter Shallow Radar (SHARAD) data for subsurface probing and surface reflectivity studies. Icarus 360, 114358. https://doi.org/10.1016/j.icarus.2021.114358.

Campbell, B.A., Watters, T.R., Morgan, G.A., 2021b. Dielectric properties of the Medusae Fossae Formation and implications for ice content. J. Geophys. Res. Planets 126. https://doi.org/10.1029/2020JE006601.

Carter, L.M., Campbell, B.A., Holt, J.W., Phillips, R.J., Putzig, N.E., Mattei, S., Seu, R., Okubo, C.H., Egan, A.F., 2009a. Dielectric properties of lava flows west of Ascraeus Mons, Mars. Geophys. Res. Lett. 36, L23204. https://doi.org/10.1029/2009GL041234.

Carter, L.M., Campbell, B.A., Watters, T.R., Phillips, R.J., Putzig, N.E., Safaeinili, A., Plaut, J.J., Okubo, C.H., Egan, A.F., Seu, R., Biccari, D., Orosei, R., 2009b. Shallow Radar (SHARAD) sounding observations of the Medusae Fossae Formation, Mars. Icarus 199, 295–302. https://doi.org/10.1016/j.icarus.2008.10.007.

Choudhary, P., Holt, J.W., Kempf, S.D., 2016. Surface clutter and echo location analysis for the interpretation of SHARAD data from Mars. IEEE Geosci. Remote Sens. Lett. 13, 1285–1289. https://doi.org/10.1109/LGRS.2016.2581799.

Christian, S., Holt, J.W., Byrne, S., Fishbaugh, K.E., 2013. Integrating radar stratigraphy with high resolution visible stratigraphy of the north polar layered deposits, Mars. Icarus 226, 1241–1251. https://doi.org/10.1016/j.icarus.2013.07.003.

Christoffersen, M.S., Holt, J.W., Kempf, S.D., O'Connell, J.D., 2021. MRO SHARAD clutter simulations data products, browse products, and documentation. NASA Planet. Data Syst. https://doi.org/10.17189/NBDH-2K53.

Courville, S.W., Perry, M.R., Putzig, N.E., 2021. Lower bounds on the thickness and dust content of layers within the north polar layered deposits of Mars from radar forward modeling. Planet. Sci. J. 2, 28. https://doi.org/10.3847/PSJ/abda50.

Cumming, I.G., Wong, F.H., 2005. Digital processing of synthetic aperture radar data: algorithms and implementation. Artech House remote sensing library, Artech House, Boston.

DiCarlofelice, A., Tognolatti, P., Bernardini, F., Putzig, N.E., 2023. A numerical model of the HF antenna of the Mars Reconnaissance Orbiter's (MRO) Shallow Radar (SHARAD) (Icarus this issue).

Foss II, F.J., Putzig, N.E., Campbell, B.A., Levin, S.A., Perry, M.R., Christoffersen, M.S., Holt, J.W., 2023. Producing 3D radargrams from orbital radar sounding data at Mars: history, methods, lessons and plans (Icarus this issue).

Foss, F.J., Putzig, N.E., Campbell, B.A., Phillips, R.J., 2017. 3-D imaging of Mars' polar ice caps using orbital radar data. Lead. Edge 36, 43–57. https://doi.org/10.1190/tle36010043.1.

Gallagher, C., Butcher, F.E.G., Balme, M., Smith, I., Arnold, N., 2021. Landforms indicative of regional warm based glaciation, Phlegra Montes, Mars. Icarus 355, 114173. https://doi.org/10.1016/j.icarus.2020.114173.

Ganesh, I., Carter, L.M., Smith, I.B., 2020. SHARAD mapping of Arsia Mons caldera. J. Volcanol. Geotherm. Res. 390, 106748 https://doi.org/10.1016/j.jvolgeores.2019.106748.

Grima, C., Kofman, W., Mouginot, J., Phillips, R.J., Hérique, A., Biccari, D., Seu, R., Cutigni, M., 2009. North polar deposits of Mars: extreme purity of the water ice. Geophys. Res. Lett. 36 https://doi.org/10.1029/2008GL036236. L03203, 4 p.

Grima, C., Kofman, W., Herique, A., Orosei, R., Seu, R., 2012. Quantitative analysis of Mars surface radar reflectivity at 20 MHz. Icarus 220, 84–99. https://doi.org/10.1016/j.icarus.2012.04.017.

Grima, C., Putzig, N.E., Campbell, B.A., Perry, M., Gulick, S.P.S., Miller, R.C., Russell, A.T., Scanlan, K.M., Steinbrügge, G., Young, D.A., Kempf, S.D., Ng, G., Buhl, D., Blankenship, D.D., 2022. Investigating the Martian surface at decametric scale: population, distribution, and dimension of heterogeneity from radar statistics. Planet. Sci. J. 3, 236. https://doi.org/10.3847/PSJ/ac9277.

Holt, J.W., Safaeinili, A., Plaut, J.J., Head, J.W., Phillips, R.J., Seu, R., Kempf, S.D., Choudhary, P., Young, D.A., Putzig, N.E., Biccari, D., Gim, Y., 2008. Radar sounding evidence for buried glaciers in the southern mid-latitudes of Mars. Science 322, 1235–1238. https://doi.org/10.1126/science.1164246.

Holt, J.W., Fishbaugh, K.E., Byrne, S., Christian, S., Tanaka, K., Russell, P.S., Herkenhoff, K.E., Safaeinili, A., Putzig, N.E., Phillips, R.J., 2010. The construction of Chasma Boreale on Mars. Nature 465, 446–449. https://doi.org/10.1038/nature09050.

Hynek, B.M., Phillips, R.J., Arvidson, R.E., 2003. Explosive volcanism in the Tharsis region: global evidence in the Martian geologic record. J. Geophys. Res. Planets 108. https://doi.org/10.1029/2003JE002062.

I-MIM MDT, 2022. Final report of the International Mars Ice Mapper Reconnaissance/ Science Measurement Definition Team.. Available online at. https://science.nasa.gov/researchers/ice-mapper-measurement-definition-team.

Jawin, E.R., Campbell, B.A., Whitten, J.L., Morgan, G.A., 2022. The lateral continuity and vertical arrangement of dust layers in the Martian north polar cap from SHARAD multiband data. Geophys. Res. Lett. 49 https://doi.org/10.1029/2022GL099896.

Kerber, L., Head, J.W., 2010. The age of the Medusae Fossae Formation: evidence of Hesperian emplacement from crater morphology, stratigraphy, and ancient lava contacts. Icarus 206, 669–684. https://doi.org/10.1016/j.icarus.2009.10.001.

Kerber, L., Head, J.W., 2012. A progression of induration in Medusae Fossae Formation transverse aeolian ridges: evidence for ancient aeolian bedforms and extensive reworking. Earth Surf. Process. Landf. 37, 422–433. https://doi.org/10.1002/esp.2259.

Kerber, L., Head, J.W., Madeleine, J.-B., Forget, F., Wilson, L., 2011. The dispersal of pyroclasts from Apollinaris Patera, Mars: implications for the origin of the Medusae Fossae Formation. Icarus 216, 212–220. https://doi.org/10.1016/j.icarus.2011.07.035.

Kreslavsky, M.A., Head, J.W., 2000. Kilometer-scale roughness of Mars: results from MOLA data analysis. J. Geophys. Res. 105, 26,695–26,711. https://doi.org/10.1029/2000JE001259.

Lalich, D.E., Holt, J.W., Smith, I.B., 2019. Radar reflectivity as a proxy for the dust content of individual layers in the Martian north polar layered deposits. J. Geophys. Res. Planets 124, 1690–1703. https://doi.org/10.1029/2018JE005787.

Lester, M., Sanchez-Cano, B., Potts, D., Lillis, R., Cartacci, M., Bernardini, F., Orosei, R., Perry, M., Putzig, N., Campbell, B., Blelly, P., Milan, S., Opgenoorth, H., Witasse, O., Redrojo, E.M.M., Russell, A., 2022. The impact of energetic particles on the Martian ionosphere during a full solar cycle of radar observations: radar blackouts. J. Geophys. Res. Space Physics 127. https://doi.org/10.1029/2021JA029535.

Mastrogiuseppe, M., Raguso, M.C., Seu, R., Putzig, N.E., 2019. Surface clutter suppression using coherent processing of radar sounder data from repeated ground tracks. 50th Lunar Planet. Sci. Conf. Abs., 2967.

Mendillo, M., Narvaez, C., Campbell, B., 2017. The total electron content of the Martian ionosphere from MRO/SHARAD observations. J. Geophys. Res. Planets 122, 2182–2192. https://doi.org/10.1002/2017JE005391.

Mishev, I., Smith, I.B., 2022. Measuring sediments of western Valles Marineris using imagery, radar, and neural networks to constrain past wet environments. 53rd Lunar Planet. Sci. Conf. Abs. 2774.

Morgan, G.A., Campbell, B.A., Carter, L.M., Plaut, J.J., Phillips, R.J., 2013. 3D reconstruction of the source and scale of buried young flood channels on Mars. Science 340, 607–610. https://doi.org/10.1126/science.1234787.

Morgan, G.A., Campbell, B.A., Carter, L.M., Plaut, J.J., 2015. Evidence for the episodic erosion of the Medusae Fossae Formation preserved within the youngest volcanic province on Mars. Geophys. Res. Lett. 42, 7336–7342. https://doi.org/10.1002/2015GL065017.

Morgan, G.A., Putzig, N.E., Perry, M.R., Sizemore, H.G., Bramson, A.M., Petersen, E.I., Bain, Z.M., Baker, D.M.H., Mastrogiuseppe, M., Hoover, R.H., Smith, I.B., Pathare, A., Dundas, C.M., Campbell, B.A., 2021. Availability of subsurface water-ice resources in the northern mid-latitudes of Mars. Nat. Astron. 5, 230–236. https://doi.org/10.1038/s41550-020-01290-z.

Mouginis-Mark, P.J., Zimbelman, J.R., 2020. Rafted pumice: a new model for the formation of the Medusae Fossae Formation, Mars. Icarus 343, 113684. https://doi.org/10.1016/j.icarus.2020.113684.

Nerozzi, S., Holt, J.W., 2018. Earliest accumulation history of the north polar layered deposits, Mars from SHARAD. Icarus 308, 128–137. https://doi.org/10.1016/j.icarus.2017.05.027.

Neumann, G.A., Abshire, J.B., Aharonson, O., Garvin, J.B., Sun, X., Zuber, M.T., 2003. Mars Orbiter Laser Altimeter pulse width measurements and footprint-scale roughness. Geophys. Res. Lett. 30, 1561. https://doi.org/10.1029/2003GL017048.

Nunes, D.C., Smrekar, S.E., Fisher, B., Plaut, J.J., Holt, J.W., Head, J.W., Kadish, S.J., Phillips, R.J., 2011. Shallow Radar (SHARAD), pedestal craters, and the lost Martian layers: initial assessments. J. Geophys. Res. 116, E04006. https://doi.org/10.1029/2010JE003690.

Orosei, R., 2006a. Mars Reconnaissance Orbiter Shallow Radar Experiment Data Record, MRO-M-SHARAD-4-EDR-V1.0. https://doi.org/10.17189/1519482.

Orosei, R., 2006b. Mars Reconnaissance Orbiter Shallow Radar Reduced Data Record, MRO-M-SHARAD-4-RDR-V1.0. NASA Planet. Data Syst. https://doi.org/10.17189/1519543.

Perry, M.R., Foss, F.J., Russell, A.T., Bain, Z.M., Russell, M.B., Chuang, F.C., Putzig, N.E., Morgan, G.A., Campbell, B.A., 2023. Three-dimensional imaging of Deuteronilus Mensae using Mars Reconnaissance Orbiter Shallow Radar (SHARAD) observations (Icarus this issue).

Petersen, E.I., Holt, J.W., Levy, J.S., 2018. High ice purity of Martian lobate debris aprons at the regional scale: evidence from an orbital radar sounding survey in Deuteronilus and Protonilus Mensae. Geophys. Res. Lett. 45, 11,595–11,604. https://doi.org/10.1029/2018GL079759.

Phillips, R.J., Zuber, M.T., Smrekar, S.E., Mellon, M.T., Head, J.W., Tanaka, K.L., Putzig, N.E., Milkovich, S.M., Campbell, B.A., Plaut, J.J., Safaeinili, A., Seu, R., Biccari, D., Carter, L.M., Picardi, G., Orosei, R., Mohit, P.S., Heggy, E., Zurek, R.W., Egan, A.F., Giacomoni, E., Russo, F., Cutigni, M., Pettinelli, E., Holt, J.W., Leuschen, C.J., Marinangeli, L., 2008. Mars north polar deposits: stratigraphy, age, and geodynamical response. Science 320, 1182–1185. https://doi.org/10.1126/science.1157546.

Phillips, R.J., Davis, B.J., Tanaka, K.L., Byrne, S., Mellon, M.T., Putzig, N.E., Haberle, R.M., Kahre, M.A., Campbell, B.A., Carter, L.M., 2011. Massive CO_2 ice deposits sequestered in the south polar layered deposits of Mars. Science 332, 838–841. https://doi.org/10.1126/science.1203091.

Picardi, G., Biccari, D., Seu, R., Plaut, J., Johnson, W.T.K., Jordan, R.L., Safaeinili, A., Gurnett, D.A., Huff, R., Orosei, R., Bombaci, O., Calabrese, D., Zampolini, E., 2004. MARSIS: Mars Advanced Radar for Subsurface and Ionosphere Sounding. In: Wilson, A. (Ed.), Mars Express: A European Mission to the Red Planet, Eur. Space Ageny Spec. Publ. ESA SP-1240, pp. 51–69.

Picardi, G., Plaut, J.J., Biccari, D., Bombaci, O., Calabrese, D., Cartacci, M., Cicchetti, A., Clifford, S.M., Edenhofer, P., Farrell, W.M., Federico, C., Frigeri, A., Gurnett, D.A., Hagfors, T., Heggy, E., Herique, A., Huff, R.L., Ivanov, A.B., Johnson, W.T.K., Jordan, R.L., Kirchner, D.L., Kofman, W., Leuschen, C.J., Nielsen, E., Orosei, R., Pettinelli, E., Phillips, R.J., Plettemeier, D., Safaeinili, A., Seu, R., Stofan, E.R., Vannaroni, G., Watters, T.R., Zampolini, E., 2005. Radar soundings of the subsurface of Mars. Science 310, 1925–1928.

Plaut, J.J., Picardi, G., Safaeinili, A., Ivanov, A.B., Milkovich, S.M., Cicchetti, A., Kofman, W., Mouginot, J., Farrell, W.M., Phillips, R.J., Clifford, S.M., Frigeri, A., Orosei, R., Federico, C., Williams, I.P., Gurnett, D.A., Nielsen, E., Hagfors, T., Heggy, E., Stofan, E.R., Plettemeier, D., Watters, T.R., Leuschen, C.J., Edenhofer, P., 2007. Subsurface radar sounding of the south polar layered deposits of Mars. Science 316, 92–95.

Plaut, J.J., Safaeinili, A., Holt, J.W., Phillips, R.J., Head III, J.W., Seu, R., Putzig, N.E., Frigeri, A., 2009. Radar evidence for ice in lobate debris aprons in the mid-northern latitudes of Mars. Geophys. Res. Lett. 36 https://doi.org/10.1029/2008GL036379. L02203.

Putzig, N.E., Phillips, R.J., Campbell, B.A., Holt, J.W., Plaut, J.J., Carter, L.M., Egan, A.F., Bernardini, F., Safaeinili, A., Seu, R., 2009. Subsurface structure of Planum Boreum from Mars Reconnaissance Orbiter Shallow Radar soundings. Icarus 204, 443–457. https://doi.org/10.1016/j.icarus.2009.07.034.

Putzig, N.E., Phillips, R.J., Campbell, B.A., Mellon, M.T., Holt, J.W., Brothers, T.C., 2014. SHARAD soundings and surface roughness at past, present, and proposed landing sites on Mars: reflections at Phoenix may be attributable to deep ground ice. J. Geophys. Res. 119, 1936–1949. https://doi.org/10.1002/2014JE004646.

Putzig, N.E., Morgan, G.A., Campbell, B.A., Grima, C., Smith, I.B., Phillips, R.J., Golombek, M.P., 2017. Radar-derived properties of the InSight landing site in western Elysium Planitia on Mars. Space Sci. Rev. 211, 135–146. https://doi.org/10.1007/s11214-016-0322-8.

Putzig, N.E., Smith, I.B., Perry, M.R., Foss, F.J., Campbell, B.A., Phillips, R.J., Seu, R., 2018. Three-dimensional radar imaging of structures and craters in the Martian polar caps. Icarus 308, 138–147. https://doi.org/10.1016/j.icarus.2017.09.023.

Putzig, N.E., Foss II, F.J., Campbell, B.A., Holt, J.W., Perry, M.R., Smith, I.B., Russell, A.T., Nerozzi, S., Christoffersen, M.S., Mueller, I.H., Sava, P.C., 2022. New views of the internal structure of Planum Boreum from enhanced 3D imaging of Mars Reconnaissance Orbiter Shallow Radar data. Planet Sci. J. 3 https://doi.org/10.3847/PSJ/ac9d3b, 14 pp.

Putzig, N.E., Morgan, G.A., Bain, Z.M., Baker, D.M.H., Bramson, A.M., Campbell, B.A., Courville, S.A., Dundas, C.M., Hoover, R.H., Mellon, M.T., Mastrogiuseppe, M., Nerozzi, S., Pathare, A.V., Perry, M.R., Petersen, E.I., Sizemore, H.G., Seu, R., Smith, I.B., 2023. Ice resource mapping on Mars. In: Badescu, V., Zacny, K., Bar-Cohen, Y. (Eds.), Handbook of Space Resources. Springer. https://doi.org/10.1007/978-3-030-97913-3_16.

Raguso, M.C, Mastrogiuseppe, M., Gambacorta, L., Di Achille, G., Seu, R., 2023. Range resolution enhancement of SHAllow RADar (SHARAD) data via bandwidth extrapolation technique: enabling new features detection and improving geophysical investigation. (Icarus this issue).

Raguso, M.C., Mastrogiuseppe, M., Seu, R., Piazzo, L., 2018. Super resolution and interferences suppression techniques applied to SHARAD data. In: 5th IEEE Intl. Wkshp. Metrology for AeroSpace. https://doi.org/10.1109/MetroAeroSpace.2018.8453529.

Ramsdale, J.D., Balme, M.R., Conway, S.J., Gallagher, C., van Gasselt, S.A., Hauber, E., Orgel, C., Séjourné, A., Skinner, J.A., Costard, F., Johnsson, A., Losiak, A., Reiss, D., Swirad, Z.M., Keresztúri, A., Smith, I.B., Platz, T., 2017. Grid-based mapping: a method for rapidly determining the spatial distributions of small features over very large areas. Planet Space Sci. 140, 49–61. https://doi.org/10.1016/j.pss.2017.04.002.

Restano, M., Plaut, J.J., Campbell, B.A., Gim, Y., Nunes, D., Bernardini, F., Egan, A., Seu, R., Phillips, R.J., 2015. Effects of the passage of comet C/2013 A1 (Siding Spring) observed by the Shallow Radar (SHARAD) on Mars Reconnaissance Orbiter. Geophys. Res. Lett. https://doi.org/10.1002/2015GL064150.

Rezza, C.A., 2021. Constraining the Hydration State of the Phyllosilicate Deposits of Eastern Valles Marineris Mars. MSc thesis. York University.

Ruff, S.W., Christensen, P.R., 2002. Bright and dark regions on Mars: particle size and mineralogical characteristics based on thermal emission spectrometer data. J. Geophys. Res. Planets 107. https://doi.org/10.1029/2001JE001580, 2-1-2–22.

Schultz, P.H., Lutz, A.B., 1988. Polar wandering of Mars. Icarus 73, 91–141. https://doi.org/10.1016/0019-1035(88)90087-5.

Séjourné, A., Costard, F., Swirad, Z.M., Łosiak, A., Bouley, S., Smith, I., Balme, M.R., Orgel, C., Ramsdale, J.D., Hauber, E., Conway, S.J., Gasselt, S., Reiss, D., Johnsson, A., Gallagher, C., Skinner, J.A., Keresztúri, Á., Platz, T., 2019. Grid mapping the Northern Plains of Mars: using morphotype and distribution of ice-related landforms to understand multiple ice-rich deposits in Utopia Planitia. J. Geophys. Res. Planets 124, 483–503. https://doi.org/10.1029/2018JE005665.

Seu, R., Biccari, D., Orosei, R., Lorenzoni, L.V., Phillips, R.J., Marinangeli, L., Picardi, G., Masdea, A., Zampolini, E., 2004. SHARAD: the MRO 2005 Shallow Radar. Planet. Space Sci. 52, 157–166. https://doi.org/10.1016/j.pss.2003.08.024.

Seu, R., Phillips, R.J., Alberti, G., Biccari, D., Bonaventura, F., Bortone, M., Calabrese, D., Campbell, B.A., Cartacci, M., Carter, L.M., Catallo, C., Croce, A., Croci, R., Cutigni, M., Di Placido, A., Dinardo, S., Federico, C., Flamini, E., Fois, F., Frigeri, A., Fuga, O., Giacomoni, E., Gim, Y., Guelfi, M., Holt, J.W., Kofman, W., Leuschen, C.J., Marinangeli, L., Marras, P., Masdea, A., Mattei, S., Mecozzi, R., Milkovich, S.M., Morlupi, A., Mouginot, J., Orosei, R., Papa, C., Paterno, T., Persi del Marmo, P., Pettinelli, E., Pica, G., Picardi, G., Plaut, J.J., Provenziani, M., Putzig, N.E., Russo, F., Safaeinili, A., Salzillo, G., Santovito, M.R., Smrekar, S.E., Tattarletti, B., Vicari, B., 2007a. Accumulation and erosion of Mars' south polar layered deposits. Science 317, 1715–1718. https://doi.org/10.1126/science.1144120.

Seu, R., Phillips, R.J., Biccari, D., Orosei, R., Masdea, A., Picardi, G., Safaeinili, A., Campbell, B.A., Plaut, J.J., Marinangeli, L., Smrekar, S.E., Nunes, D.C., 2007b. SHARAD sounding radar on the Mars Reconnaissance Orbiter. J. Geophys. Res. 112, E05S05. https://doi.org/10.1029/2006JE002745.

Shoemaker, E.S., Carter, L.M., Garry, W.B., Morgan, G.A., Plaut, J.J., 2022. New insights into subsurface stratigraphy northwest of Ascraeus Mons, Mars, using the SHARAD and MARSIS radar sounders. J. Geophys. Res. Planets 127. https://doi.org/10.1029/2022JE007210.

Simon, M.N., Carter, L.M., Campbell, B.A., Phillips, R.J., Mattei, S., 2014. Studies of lava flows in the Tharsis region of Mars using SHARAD. J. Geophys. Res. Planets 119, 2291–2299. https://doi.org/10.1002/2014JE004666.

Smith, I.B., Holt, J.W., 2010. Onset and migration of spiral troughs on Mars revealed by orbital radar. Nature 465, 450–453. https://doi.org/10.1038/nature09049.

Smith, I.B., Holt, J.W., 2015. Spiral trough diversity on the north pole of Mars, as seen by Shallow Radar (SHARAD). J. Geophys. Res. 120, 362–387. https://doi.org/10.1002/2014JE004720.

Smith, I.B., Spiga, A., Holt, J.W., 2015. Aeolian processes as drivers of landform evolution at the south pole of Mars. Geomorphology 240, 54–69. https://doi.org/10.1016/j.geomorph.2014.08.026.

Smith, I.B., Putzig, N.E., Holt, J.W., Phillips, R.J., 2016. An ice age recorded in the polar deposits of Mars. Science 352, 1075–1078. https://doi.org/10.1126/science.aad6968.

Squyres, S.W., 1979. The distribution of lobate debris aprons and similar flows on Mars. J. Geophys. Res. 84, 8087. https://doi.org/10.1029/JB084iB14p08087.

Stuurman, C.M., Osinski, G.R., Holt, J.W., Levy, J.S., Brothers, T.C., Kerrigan, M., Campbell, B.A., 2016. SHARAD detection and characterization of subsurface water ice deposits in Utopia Planitia, Mars. Geophys. Res. Lett. 43, 9484–9491. https://doi.org/10.1002/2016GL070138.

Tanaka, K.L., Fortezzo, C.M., 2012. Geologic Map of the North Polar Region of Mars. U.S. Geological Survey Scientific Investigations Map 3177.

Watters, T.R., Campbell, B., Carter, L., Leuschen, C.J., Plaut, J.J., Picardi, G., Orosei, R., Safaeinili, A., Clifford, S.M., Farrell, W.M., 2007. Radar sounding of the Medusae Fossae Formation Mars: equatorial ice or dry, low-density deposits? Science 318, 1125–1128.

Whitten, J.L., Campbell, B.A., 2018. Lateral continuity of layering in the Mars south polar layered deposits from SHARAD sounding data. J. Geophys. Res. Planets 123, 1541–1554. https://doi.org/10.1029/2018JE005578.

Whitten, J.L., Campbell, B.A., Morgan, G.A., 2017. A subsurface depocenter in the south polar layered deposits of Mars. Geophys. Res. Lett. 44, 8188–8195. https://doi.org/10.1002/2017GL074069.

Zimbelman, J.R., Griffin, L.J., 2010. HiRISE images of yardangs and sinuous ridges in the lower member of the Medusae Fossae Formation, Mars. Icarus 205, 198–210. https://doi.org/10.1016/j.icarus.2009.04.003.

Zimbelman, J.R., Scheidt, S.P., 2012. Hesperian age for western Medusae Fossae Formation, Mars. Science 336, 1683. https://doi.org/10.1126/science.1221094.